Nanoscale

PAPER

View Article Online
View Journal | View Issue

Cite this: *Nanoscale*, 2023, **15**, 2924

Efficient thin-film perovskite solar cells from a two-step sintering of nanocrystals†

Yuhao Peng,‡ Junli Huang,‡ Lue Zhou,‡ Yuncheng Mu, Shuyao Han, Shu Zhou * and Pingqi Gao *

Received 2nd December 2022,
Accepted 18th January 2023

DOI: 10.1039/d2nr06745e

rsc.li/nanoscale

Creating semiconductor thin films from sintering of colloidal nanocrystals (NCs) represents a very important technology for high throughput and low cost thin-film photovoltaics. Here we report the creation of all-inorganic cesium lead bromide ($CsPbBr_3$) polycrystalline films with grain size exceeding 1 μm from the bottom up by sintering of $CsPbBr_3$ NCs terminated with short and low-boiling-point alky ligands that are ideal for use in sintered photovoltaics. The grain growth behavior during the sintering process was carefully investigated and correlated to the solar cell performance. To achieve precise control over the microstructural development we propose a facile two-step sintering process involving the grain growth *via* coarsening at a relative low temperature followed by densification at a high temperature. Compared with the one-step sintering, the two-step process yields a more uniform $CsPbBr_3$ bulk film with larger grain size, higher density and lower trap density. Consequently, the photovoltaic device based on the two-step sintering process demonstrates a significant enhancement of efficiency with reduced hysteresis that approaches the best reported $CsPbBr_3$ solar cells using a similar configuration. Our study specifies a rarely addressed perspective concerning the sintering mechanism of perovskite NCs and should contribute to the development of high-performance bulk perovskite devices based on the building blocks of perovskite NCs.

Introduction

Halide perovskites have bourgeoned in the field of photovoltaics in the past decade.[1,2] The capacity to manipulate the microstructure and morphology of halide perovskite films is critical in achieving a high power conversion efficiency (PCE) in addition to chemical innovation, *i.e.*, designing composition and crystal structure.[3,4] Current progress in perovskite solar cells largely benefits from the advance of solution methods in promoting the microstructure and morphology.[5–7] A one-step spin-coating method was firstly employed to prepare $MAPbI_3$ perovskite solar cells, showing an initial efficiency of 3.8% due to the dendritic morphology with poor coverage.[8] Subsequently, a modified one-step method involving the use of antisolvents was proposed to improve the film morphology by promoting the crystallization process.[9,10] Meanwhile, a two-step spin-coating method consisting of sequential depositions of an inorganic lead halide layer and an organic salt was developed, yielding a uniform, compact and pin-hole-free perovskite film and thereby a high PCE of 25.6%.[11] Unlike hybrid perovskites containing organic components, however, the fabrication of all-inorganic perovskite films is challenging by using conventional solution methods. For instance, the solubility of CsBr is rather poor in organic solvents, making typical solution deposition methods difficult to adapt for constructing bulk $CsPbBr_3$ devices.[12–14]

Formation of semiconductor thin films from sintering of colloidal nanocrystals (NCs) represents an important and complementary technology for high throughput and low cost thin-film photovoltaics.[15,16] Manipulating the sintering process also allows precise control over the microstructure development, which makes attainment of desired microstructure and morphology possible. Typical colloidal semiconductor NCs such as CdTe and CuInGaSe have been demonstrated in sintered photovoltaics, yielding an impressive PCE exceeding 17% on a par with their bulk counterparts.[17–19] Recently, Kamat *et al.* have shown fabrication of $CsPbBr_3$ bulk films by thermal annealing of $CsPbBr_3$ NCs that are surface terminated with long organic ligands, *i.e.*, oleic acid and oleylamine.[20,21] However, it is found that the transformation from NCs into bulk during thermal annealing arises from the resumption of nanoparticle growth rather than from sintering as assumed. Additionally, the tightly bound bulky ligands may reside in the sintered film and impact the grain growth, therefore not be ideal for use in sintered photovoltaics. Beyond

School of Materials, Shenzhen Campus of Sun Yat-Sen University, Shenzhen, Guangdong 518107, China.
E-mail: zhoush67@mail.sysu.edu.cn, gaopq3@mail.sysu.edu.cn

†Electronic supplementary information (ESI) available. See DOI: https://doi.org/10.1039/d2nr06745e

‡These authors contribute equally to this work.

photovoltaics, Bennett *et al.* reported liquid-phase sintering of $CsPbI_3$ particles and metal–organic framework glasses which show superior optical stability against to heat, light, air, and ambient humidity.[22] A room-temperature mechanical sintering process for $MAPbI_3$ microcrystals was employed by Brabec *et al.* to form polycrystalline wafers with thickness ranging from 0.2 to 1 mm under a pressure of 0.3 GPa.[23] Despite recent progress made on sintered perovskite structures, however, there have been few attempts to understand the sintering mechanism and development of thin-film solar cells from sintering of perovskite NCs is still in its infancy.

In this work, colloidal $CsPbBr_3$ NCs terminated with low-boiling-point alky ligands were proposed as building blocks to construct thin-film solar cells from the bottom up by sintering. The grain growth behavior of $CsPbBr_3$ NCs was carefully investigated and correlated to the solar cell performance. It is found that the traditional terms used to describe the sintering process of porous ceramics could also be applied to perovskite NCs. The sintering not only leads to grain growth *via* coarsening and closing of pores in terms of densification that are beneficial for device application, but also unwanted impurity phase, *i.e.*, lead carbonate ($PbCO_3$), impeding the device performance. Inspired by the progress in the sintering of ceramics,[24,25] we propose a facile two-step sintering process to achieve precise control over the microstructure development by augmentation of coarsening and suppression of both pores and impurity phases. Solar cells based on the bulk films from the two-step sintering process show a significant enhancement of the PCE compared with conventional one-step process. Our study suggests a feasible strategy for the construction of efficient thin-film perovskite devices based on the building blocks of colloidal perovskite NCs.

Results and discussion

Strongly-emissive colloidal $CsPbBr_3$ NCs terminated with low-boiling-point and short alkyl ligands were synthesized by using a room-temperature method reported previously with little modification (Fig. S1†).[26] Transmission electronic microscopy (TEM) image shows that the obtained $CsPbBr_3$ NCs are roughly 10–20 nm in size. X-ray diffraction (XRD) measurement demonstrates the $CsPbBr_3$ NCs are highly crystallized with an orthorhombic structure (Fig. S1†). The optical absorption spectrum of $CsPbBr_3$ NCs features a well-defined excitonic peak at ~512 nm (Fig. S1†). The corresponding photoluminescence (PL) peak locates at ~518 nm with a relatively small full-width at half-maximum (FWHM, ~20 nm), suggesting the NCs has a narrow size distribution.

Beneficial from the short ligands at the NC surface, the as-synthesized $CsPbBr_3$ NCs could be directly employed for solution-processed device applications. Fig. S2† schematically shows the layer-by-layer deposition method for fabricating $CsPbBr_3$-NC films. The spincoating process can be repeated to creat films with different thickness (Fig. S3†). Schematic of the solar cell structure based on as-synthesized $CsPbBr_3$ NCs was shown in Fig. 1a. With a three-cycle spin-coating step of the suspended $CsPbBr_3$-NC ink on a c-TiO_2 substrate, a complete coverage of the substrate could be obtained (Fig. S4†). The solar cell device, in this case, exhibited a short-circuit value (J_{sc}) of 1.26 mA cm^{-2}, an open-circuit voltage (V_{oc}) of 0.87 V, and a fill factor (FF) of 0.65, leading to a PCE of 0.72% (Fig. S5†). It can be seen that the low PCE largely stems from the low photocurrent because the NC film is very thin. A thicker film is thus demanded which could be obtained by simply increasing the deposition cycles when spincoating the NC ink. As the deposition cycle increases, however, it is found that the current density–voltage (J–V) curves of the solar cells remain almost unchanged (Fig. 1b). Both the J_{sc} and V_{oc} are independent on the film thicness (Table S1†). This is possibly due to the existence of ligands at the $CsPbBr_3$-NC surface which limits the electronic coupling of NCs, and thereby the carrier transport between perovskite NCs.[27]

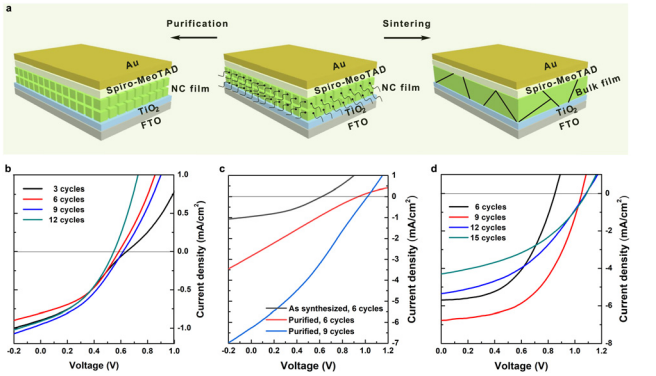

Fig. 1 (a) Schematic showing the evolution of $CsPbBr_3$ solar cell structures after purification and sintering. (b–d) Current density–voltage curves of the $CsPbBr_3$ solar cells as a function of the deposition cycles measured under standard AM 1.5 conditions. Current density–voltage curves were recorded at a scan rate of 0.1 V s^{-1} in the forward direction. (b) As-synthesized, (c) purified, (d) sintered.

To improve the device performance, two different methods, *i.e.*, chemical purification and thermal sintering, were employed to eliminate the negative impact of surface ligands. Firstly, the $CsPbBr_3$ NCs were purified by washing in toluene for two times to remove the organic ligands. The electrical conductivity of the NC film readily increases after purification. Both the J_{sc} and V_{oc} remarkably increase with the deposition cycles (Fig. 1c). This means that the carrier transport between $CsPbBr_3$ NCs has been greatly improved. However, a S-shape characteristic occurs to the J–V curve, resulting in a significant drop of the FF. The S-shape J–V curve suggests removing of alky ligands by purification results in exposure of more under-coordinated surface defects, and thereby an increased non-radiative recombination (Fig. S6†).[28] Such S-shape J–V curves were not observed for the $CsPbBr_3$ films after sintering. Fig. 1d representatively shows the results for the films after sintering at 280 °C. It is seen that the FF is clearly improved compared with the devices based on the purified $CsPbBr_3$ NCs. In addition, both the V_{oc} and J_{sc} markedly changes with the film

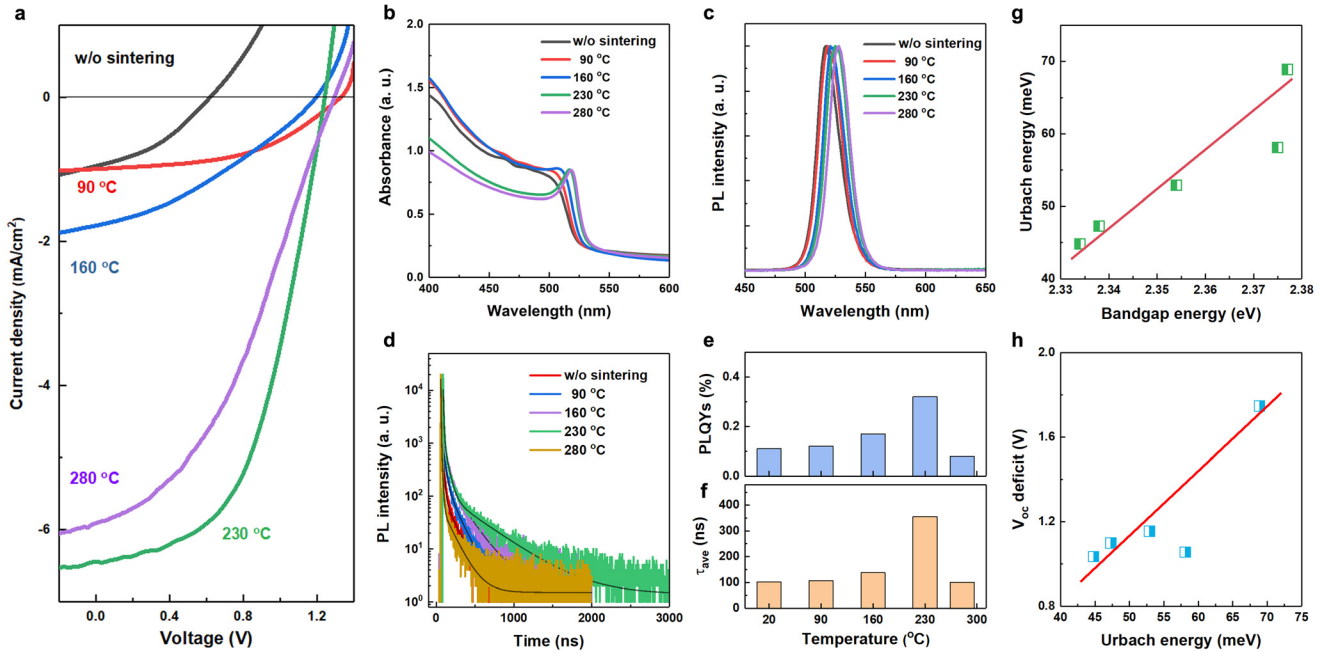

Fig. 2 (a) Current density–voltage curves of the $CsPbBr_3$ solar cells as a function of the sintering temperature measured under standard AM 1.5 condition. Current density–voltage curves were recorded at a scan rate of 0.1 V s^{-1} in the forward direction. (b) UV-vis absorption spectra of $CsPbBr_3$-NC films after sintering at different temperature. (c) Steady-state and (d) time-resolved PL results of the $CsPbBr_3$-NC films after sintering at different temperature. The sintering time for all samples is 2 h. (e) PLQYs and (f) τ_{ave} *versus* sintering temperature. (g) Urbach energy (E_U) *versus* bandgap energy (E_g) obtained from the absorption spectra for the $CsPbBr_3$-NC films after sintering at different temperature. (h) V_{oc} deficit (defined as $E_g/e - V_{oc}$) of $CsPbBr_3$ solar cells *versus* E_U of corresponding $CsPbBr_3$ films. The solid lines in g and h are drawn to guide the eye.

thickness. These results imply that the surface ligands could be eliminated without the creation of extra defects by sintering.

The temperature was then optimized to signify a positive role of sintering in $CsPbBr_3$ solar cells. Fig. 2a shows *J–V* curves of the solar cells after sintering at different temperatures. A gradual increase of the efficiency with the temperature is observed when the temperature is lower than 230 °C. For films sintered at 280 °C, however, the efficiency is actually reduced. Compared with the V_{oc} and FF, the J_{sc} is found to be more seriously impacted by the sintering temperature (Fig. S7 and Table S2†). Charge-carrier dynamics are known in close relation to the performance of solar cells based on perovskite films. To understand the correlation between device performance and sintering temperature, both steady-state and time-resolved optical measurements were performed. Fig. 2b shows normalized UV-vis absorption spectra of the $CsPbBr_3$-NC films. It is seen that the excitonic absorption peak becomes prominent after sintering and monotonically red-shifts with the increase of temperature, suggesting the growth of large sized particles. In the meantime, the steady-state photoluminescence (PL) peak gradually shifts toward a lower energy (Fig. 2c). Fig. 2d shows time-resolved PL spectra for the $CsPbBr_3$-NC films after sintering at different temperatures. All the curves exhibit a tri-exponential decay behavior involving three components of lifetime (Fig. S8†), which can be ascribed to Shockley–Read–Hall (SRH) recombination *via* defect trapping, radiative recombination of free electrons/holes, and Auger recombination, respectively.[29,30] The average lifetime (τ_{ave}) is related to the lifetime (τ_1, τ_2, τ_3) and fraction (B_1, B_2, B_3) of each decay component (Fig. S9†) as $\tau_{ave} = \frac{B_1\tau_1^2 + B_2\tau_2^2 + B_3\tau_3^2}{B_1\tau_1 + B_2\tau_2 + B_3\tau_3}$. As shown in Fig. 2f, the τ_{ave} increases first from 103 ns (w/o sintering) to 355 ns (230 °C), and then quickly drops to 101 ns (280 °C). Clearly, the film sintered at 230 °C has a much longer carrier lifetime, implying much fewer deep-level defects.[31] The trend of τ_{ave} variation together with the change of PL quantum yields (QYs) (Fig. 2e), coincides well with the variation of the solar cell performance (Fig. 2a).

To evaluate the electronic quality of thin films after sintering we have calculated the Urbach energy (E_U). The E_U is related to the width of the exponentially decaying sub-bandgap absorption tail which can be expressed as:

$$E_U = (E - E_g)/\ln\left(\frac{\alpha(E)}{\alpha_g}\right), \quad (1)$$

where $\alpha(E)$ is the absorption coefficient spectra and α_g is the value of α at the bandgap energy (E_g).[32] To obtain the E_g for each $CsPbBr_3$ film we employ the Tauc law to analysis the optical absorption spectra (Fig. S10 and S11†). Fig. 2g shows change of the E_U for the $CsPbBr_3$ films as a function of E_g. The values of E_U (Fig. S12†) are in good agreement with previous

reports on halide perovskite films.[33] The E_U monotonically decreases with the temperature and E_g. A lower value of E_U implies a smaller sub-bandgap absorption and fewer sub-bandgap defects. It is known that the presence of sub-bandgap defects can act as Shockley–Read–Hall recombination centers, reducing the V_{oc} of perovskite solar cells. The V_{oc} deficit has been commonly used as a device parameter to correlate with E_U which is defined as:

$$V_{oc}\ \text{deficit} = E_g/e - V_{oc}, \quad (2)$$

where e is the elemental charge.[34] A linear trend in the V_{oc} deficit *versus* E_U is observed (Fig. 2h). Previous studies on various solar cells have also shown a direct relationship between the V_{oc} deficit and E_U.[35,36] Together with the variation of E_g, they indicate an increased grain size and a reduced grain boundary in the perovskite films. However, the trend of E_U variation is not fully consistent with the evolution of carrier lifetime and solar cell efficiency when the temperature reaches 280 °C. A shorter PL lifetime should reduce the V_{oc} as a result of larger non-radiative recombination, while a smaller bandgap due to the larger gain size should give rise to a higher J_{sc}. Together, they imply a different mechanism should be responsible for the actual drop of PCE at high temperature.

To clarify the origin of the drop of PCE at higher temperature, the microstructures of $CsPbBr_3$-NC films after sintering were systematically investigated. Fig. 3a presents scanning electronic microscopy (SEM) images showing the evolution of the $CsPbBr_3$-NC film morphology upon sintering temperature and time. Before sintering, a smooth and continuous film consisting of nearly spherical perovskite NCs was clearly observed. When the temperature increases to 90 °C, the NC film became porous because of the volatilation of adsorbed solvents and short ligands. Sintering effect on the microstructure and merged grains could not be identified. This is in consistence with evolution of the optical bandgap in previous discussions. For sample sintered at 160 °C, perovskite NCs started to merge and larger grains (~150 nm) with a non-spherical shape were

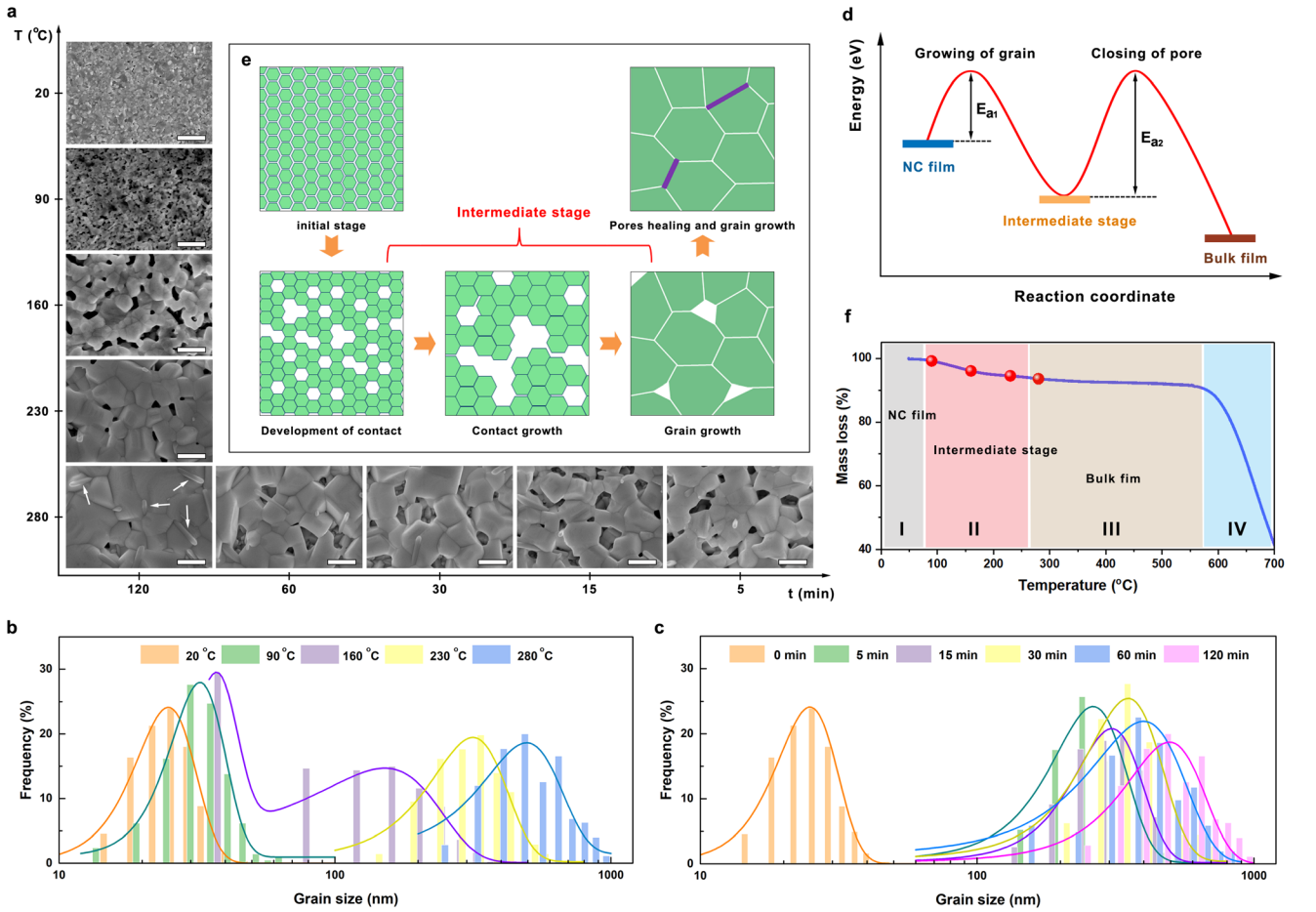

Fig. 3 (a) SEM images of $CsPbBr_3$-NC films sintered at different temperature and time. Incomplete removal of the porosity during solid-state sintering results in a microstructure consisting of grains, grain boundaries, and pores. (b) Grain growth in $CsPbBr_3$-NC films as a function of sintering temperature. (c) Grain growth in $CsPbBr_3$-NC films as a function of sintering time. (d) Schematic showing the reaction coordinate diagram for the formation of bulk perovskites from sintering of NCs. (e) Schematic diagram illustrating the microstructure and morphology evolution during the sintering process. (f) TGA curve of $CsPbBr_3$ NCs.

formed. In addition, a neck was observed between these grains. Nevertheless, spherical and small grains (~30 nm) could also be found from the SEM image, yielding a bimodal grain size distribution (Fig. 3b). Such abnormal grain growth has also been observed in the sintering process of ceramics whereby a few large grains grow rapidly at the expense of the smaller grains.[37,38] This leads to an increase in the average grain size accompanied by an increase in the average pore size in a manner similar to Ostwald ripening, which is also known as coarsening that has been frequently used to describe the growing process in porous ceramics (Fig. S13†). For $CsPbBr_3$-NC film sintered at 230 °C, grain boundaries between merged grains at 160 °C were not observed, suggesting the complete merging of small grains. Intriguingly, the pore size did not increase with the increase of the average grain size anymore. In particular, closing of the pores was observed when the temperature was further increased to 280 °C. Grains approached to each other, suggesting switching from the coarsening to a densification regime which was desired for device applications. However, new grains with a rod shape were formed and distributed in the whole film. The new impurity phase was subsequently evidenced to be $PbCO_3$ by energy dispersive X-ray spectroscopy (EDX) measurement (Fig. S14†) because $PbCO_3$ tends to form naturally when lead is released into the atmosphere upon heating. Clearly, the appearance of impurity phase exposes a negative effect on the device performance although the existence of $PbCO_3$ will not result in the complete loss of photovoltaic performance (Fig. 2a). We have also recorded the evolution of the $CsPbBr_3$-NC film morphology upon sintering time at 280 °C (Fig. 3a). It was found that the impurity phase was largely reduced with the time reduction. In addition, a rapid increase of grain size was observed in the SEM image after a short-term sintering for only 5 min. As the time increases, the size gradually increases from 300 nm to 500 nm (Fig. 3c). This implies the sintering temperature more seriously impacts the grain growth behavior than the sintering time which makes attainment of the desired microstructure possible by controlling the sintering process.

On the basis of the above results, we herein propose a possible model for the sintering of $CsPbBr_3$ NCs involving the growing of grains *via* coarsening and the closing of pores *via* densification. In general, coarsening reduces the driving force for sintering while increases the diffusion distance for matter transport, thereby reducing the rate of sintering.[39] In this context, a larger energy barrier (E_{a2}) needs to be confronted for closing of pores than that needed for grain growth (E_{a1}) (Fig. 3d). Consequently, a higher temperature is required to enable further growth and densification of the $CsPbBr_3$ film. Fig. 3e schematically shows the model for sintering of $CsPbBr_3$ NCs involving five stages, *i.e.*, initial stage, development of contact, contact growth, grain growth, and pores healing and densification, which is further underpinned by thermal stability measurement. In terms of the change of the NC mass the thermogravimetric analysis (TGA) curve can also be divided into four stages (I, II, III, and IV) accordingly (Fig. 3f). In the initial stage (T < 90 °C), the mass of the NC sample remains unchanged and the NC morphology is preserved. In the second stage (90 °C < T < 280 °C), the mass of the NC sample decreases mainly due to volatilization of alky ligands and adsorbed surface molecules given the large specific surface area.[40] In this intermediate stage, sintering effects on the microstructure such as develop of contact, contact growth and grain growth are identified. In the third stage (280 °C < T < 560 °C), the mass decrease slows down, indicating complete removal of the surface organic ligands, facilitating the formation of dense and uniform bulk films. Finally, the mass decrease accelerates due to the decomposition of perovskites at T > 560 °C.

Normally it is desired in optoelectronics to achieve as high a density, as big a grain size, and as uniform a microstructure as possible. The abnormal grain growth during sintering limits the attainment of high density because the pores trapped in the abnormal grain are difficult to be removed. In addition, the formation of impurity phase should be avoided which is commonly detrimental to the properties of halide perovskite films. To achieve precise control over the microstructure development we propose a facile two-step sintering process involving a long-term coarsening at a relative low temperature (*e.g.*, 230 °C) followed by a short-term densification at a high temperature (*e.g.*, 280 °C) (Fig. 4a). The long-

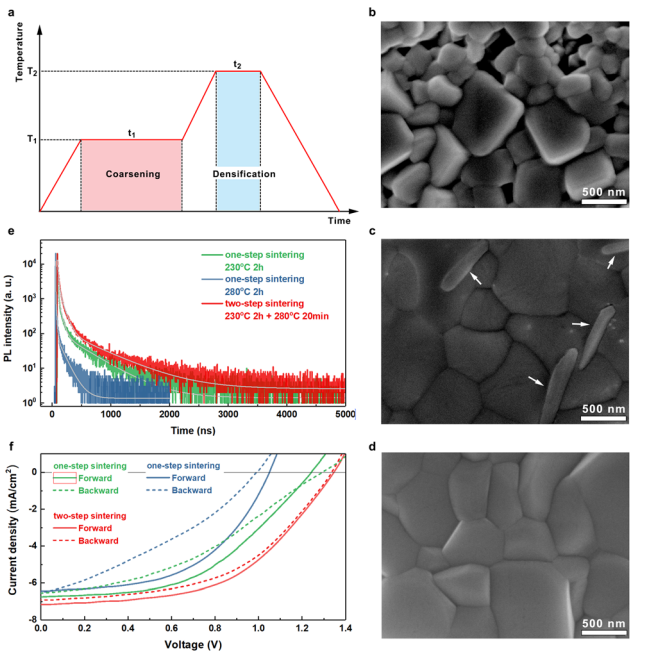

Fig. 4 (a) Illustrative representation of the two-step sintering plot. SEM images of the $CsPbBr_3$ films obtained by (b and c) one-step sintering and (d) two-step sintering. (b) 230 °C for 2 h, (c) 280 °C for 2 h, and (d) 230 °C for 2 h + 280 °C for 20 min. (e) Time-resolved PL curves of the $CsPbBr_3$ films obtained by one-step sintering and two-step sintering in (b–d). (f) Current density–voltage curves of the best $CsPbBr_3$ solar cells obtained by one-step sintering and two-step sintering measured under standard AM 1.5 conditions. Current density–voltage curves were recorded at a scan rate of 0.1 V s^{-1} in both forward and reverse directions.

term coarsening renders continuous growth of grain size while the short-term densification aims to produce a high density without the introduce of impurity grains. Compared with the one-step sintering (Fig. S15†), the two-step method yields a denser and more uniform $CsPbBr_3$ bulk film with fewer pores and larger grain size (Fig. 4b–d). Meanwhile, the impurity phase was evidenced to be significantly reduced in the XRD spectrum (Fig. S16†) and hardly identified from the SEM image (Fig. 4d). The τ_{ave} derived from the time-resolved PL curve reaches 416 ns, which is also much larger than the films from the one-step sintering (Fig. 4e). Consequently, the photovoltaic device based on the two-step sintering process demonstrates a significant enhancement (~37%) of PCE with reduced hysteresis (Fig. 4f and Table S3†). In particular, the champion device delivered a high efficiency of 5.2% which is on a par with the best reported $CsPbBr_3$ solar cells using a similar configuration (Table S4†). It is worth noting that the PCE of $CsPbBr_3$ solar cells with gold electrode typically have a PCE < 6% although gold has been frequently used for high performance hybrid perovskite solar cells.[12,26,41] Recent studies indicate that the PCE of $CsPbBr_3$ solar cells can be greatly improved to be >10% when gold electrode is replaced by carbon electrode.[42–45] It is expected that significant improvement could be further achieved through optimizing the device configuration by taking advantages of the carbon electrode for $CsPbBr_3$ solar cells.

Conclusions

In conclusion, we report development of thin-film solar cells from sintering of perovskite NCs terminated with short and low-boiling-point organic ligands. The sintering mechanism was carefully investigated and correlated to the solar cell performance systematically. Unlike perovskite NCs that are surface terminated with long organic ligands, it is found that the transformation from NCs into bulk form involves five stages, *i.e.*, initial stage, development of contact, contact growth, grain growth, and pores healing and densification, in a manner similar to the sintering process of porous ceramics. The sintering process on one side leads to grain growth *via* coarsening and closing of pores *via* densification that are beneficial for device application. On the other side, unwanted impurity phase was formed, impeding the device performance. In order to achieve precise control over the microstructure development a facile two-step sintering process is proposed, involving a long-term coarsening at a relative low temperature followed by a short-term densification at a high temperature for the sake of augmentation of grain growth and suppression of both pores and impurity phases. As a result, the photovoltaic device based on the two-step sintering process demonstrates a significant enhancement of PCE with reduced hysteresis. A high efficiency of 5.2% is obtained approaching the best reported $CsPbBr_3$ solar cells using a similar configuration and could be further improved when carbon electrode is used. Our study provides important insights into the sintering mechanism of perovskite NCs and shall open up possibilities for the construction of high performance bulk perovskite devices based on the building blocks of perovskite NCs.

Experimental section

Materials

Lead(II) bromide ($PbBr_2$, Sigma-Aldrich, 99.999%, metals basis), cesium carbonate (Cs_2CO_3, Aladdin, 99.9%, metals basis), butylamine (BuAm, Aladdin, 99.5%), 2-propanol (iPrOH, Sigma-Aldrich, anhydrous, 99.5%), propionic acid (PrAc, Aladdin, 99.5%), hexane (HEX, Sigma-Aldrich, 95%), toluene (Sigma-Aldrich, anhydrous, 99.8%), spiro-OMeTAD (Merck, 99.8%).

Synthesis of $CsPbBr_3$ NCs

The synthesis of $CsPbBr_3$ NCs is adapted from that reported in previous literature with little modification. Firstly, $PbBr_2$ precursor solution was prepared by dissolving 184 mg (0.5 mmol) $PbBr_2$ in 1 ml 1 : 1 : 1 iPrOH : PrAc : BuAm, respectively. Cs-PrAc precursor solution was prepared by dissolving 163 mg Cs_2CO_3 (0.5 mmol) in 0.5 ml PrAc. 20 μl Cs-PrAc was added into a mixed solution of hexane and 2-propanol (HEX : iPrOH = 2 : 1). 100 μl $PbBr_2$ precursor was subsequently injected and the solution quickly turned green within a few seconds. The $CsPbBr_3$ NCs were collected by centrifuging for 3 min at 1500 rpm and then re-dispersed in toluene.

Characterization

TEM images were recorded by FEI Tecnai Spirit microscope operated at an acceleration voltage of 200 kV. SEM images were recorded by using a FEI Quanta 400 field emission microscope operated at an acceleration voltage of 25 kV. Steady-state and time-resolved PL measurements were performed by using a fluorescence spectrometer (Edinburgh FLS980). A UV-vis spectrometer (Hitachi U-3501) was used to measure the optical absorption of $CsPbBr_3$ films. The TGA measurements were conducted in the atmosphere of air. Samples for the TGA measurements were powders of $CsPbBr_3$ NCs precipitated from the inks by centrifugation followed by drying in the vacuum. The samples were heated from room temperature at a heating rate of 10 °C min^{-1}.

Fabrication of solar cells

FTO glass substrates were cleaned by sonication in deionized water, isopropyl alcohol and acetone, followed by oxygen plasma treatment for 15 min. Immediately after the oxygen plasma treatment, a compact TiO_2 film was deposited onto the cleaned FTO substrate by spin coating the titanium precursor solution (0.9 mL titanium isopropoxide and 0.1 mL 37% HCl in 15 mL anhydrous ethyl alcohol) followed by annealing at 500 °C for 3 h in air. Subsequently, the substrates were transferred into a fuming cupboard for a layer-by-layer deposition of $CsPbBr_3$-NC films, followed by sintering at 90 °C, 160 °C, 230 °C and 280 °C, respectively. The increase rate of tempera-

ture for sintering was controlled to be 30 °C min^{-1}. A spiro-MeOTAD film was then coated onto the $CsPbBr_3$ film using a spin speed of 1500 rpm from a 15 mg ml^{-1} chlorobenzene solution. After oxidation in dry air a 100 nm Au top electrode was finally deposited by thermal evaporation.

Electrical measurements

Current density–voltage (*J–V*) measurements were performed in a nitrogen-purged glove box under dark condition and AM 1.5G solar illumination at 100 mW cm^{-2} by using a Keithley 2612 source meter with a scanning rate of 0.1 V s^{-1}. The device area is 0.045 cm^2.

Author contributions

S. Zhou conceived the idea. J. Huang, Y. Peng, and L. Zhou conducted the experiments and coordinated the experiments. S. Zhou wrote the manuscript. All authors discussed and commented on the paper.

Conflicts of interest

There are no conflicts to declare.

Acknowledgements

This work is mainly supported by the National Natural Science Foundation of China (Grant No. 62004230) and the Science and Technology Innovation Commission of Shenzhen (Grant No. GXWD20200830152356001).

Notes and references

1 M. A. Green, A. Ho-Baillie and H. J. Snaith, The emergence of perovskite solar cells, *Nat. Photonics*, 2014, **8**(7), 506.
2 T. Miyasaka, A decade of perovskite photovoltaics, *Nat. Energy*, 2019, **4**(1), 1.
3 N. J. Jeon, J. H. Noh, W. S. Yang, Y. C. Kim, S. Ryu, J. Seo and S. I. Seok, Compositional engineering of perovskite materials for high-performance solar cells, *Nature*, 2015, **517**(7535), 476.
4 M. Saliba, T. Matsui, K. Domanski, J. Y. Seo, A. Ummadisingu, S. M. Zakeeruddin, J. P. Correa-Baena, W. R. Tress, A. Abate, A. Hagfeldt, *et al.*, Incorporation of rubidium cations into perovskite solar cells improves photovoltaic performance, *Science*, 2016, **354**(6309), 206.
5 J. Yuan, A. Hazarika, Q. Zhao, X. Ling, T. Moot, W. Ma and J. M. Luther, Metal halide perovskites in quantum dot solar cells: progress and prospects, *Joule*, 2020, **4**, 1160–1185.
6 J. Burschka, N. Pellet, S. J. Moon, R. Humphry-Baker, P. Gao, M. K. Nazeeruddin and M. Gratzel, Sequential deposition as a route to high-performance perovskite-sensitized solar cells, *Nature*, 2013, **499**(7458), 316.
7 T. Liu, Y. Zhou, Q. Hu, K. Chen, Y. Zhang, W. Yang, J. Wu, F. Ye, D. Luo, K. Zhu, N. Padture, F. Liu, T. Russell, R. Zhu and Q. Gong, Fabrication of compact and stable perovskite films with optimized precursor composition in the fast-growing procedure, *Sci. China Mater.*, 2017, **60**, 608–616.
8 A. Kojima, K. Teshima, Y. Shirai and T. Miyasaka, Organometal halide perovskites as visible-light sensitizers for photovoltaic cells, *J. Am. Chem. Soc.*, 2009, **13**(17), 6050.
9 N. Ahn, D.-Y. Son, I.-H. Jang, S. M. Kang, M. Choi and N.-G. Park, Highly reproducible perovskite solar cells with average efficiency of 18.3% and best efficiency of 19.7% fabricated via lewis base adduct of lead(II) iodide, *J. Am. Chem. Soc.*, 2015, **137**(27), 8696.
10 N. J. Jeon, J. H. Noh, Y. C. Kim, W. S. Yang, S. Ryu and S. I. Seok, Solvent engineering for high-performance inorganic–organic hybrid perovskite solar cells, *Nat. Mater.*, 2014, **13**(9), 897.
11 Y. Zhao, F. Ma, Z. Qu, S. Yu, T. Shen, H.-X. Deng, X. Chu, X. Peng, Y. Yuan, X. Zhang and J. You, Inactive $(PbI_2)_2RbCl$ stabilizes perovskite films for efficient solar cells, *Science*, 2022, **377**(6605), 531.
12 M. Kulbak, D. Cahen and G. Hodes, How important is the organic part of lead halide perovskite photovoltaic cells? Efficient $CsPbBr_3$ cells, *J. Phys. Chem. Lett.*, 2015, **6**(13), 2452.
13 D. W. Huang, P. F. Xie, Z. X. Pan, H. S. Rao and X. H. Zhong, One-step solution deposition of $CsPbBr_3$ based on precursor engineering for efficient all-inorganic perovskite solar cells, *J. Mater. Chem. A*, 2019, **7**(39), 22420.
14 J. H. Li, L. M. Xu, T. Wang, J. Z. Song, J. W. Chen, J. Xue, Y. H. Dong, B. Cai, Q. S. Shan, B. N. Han and H. B. Zeng, 50-fold EQE improvement up to 6.27% of solution-processed all-inorganic perovskite $CsPbBr_3$ QLEDs via surface ligand density control, *Adv. Mater.*, 2017, **29**, 1603885.
15 C. N. Bucherl, K. R. Oleson and H. W. Hillhouse, Thin film solar cells from sintered nanocrystals, *Curr. Opin. Chem. Eng.*, 2013, **2**(2), 168.
16 C. J. Stolle, T. B. Harvey and B. A. Korgel, Nanocrystal photovoltaics: a review of recent progress, *Curr. Opin. Chem. Eng.*, 2013, **2**(2), 160.
17 B. I. MacDonald, A. Martucci, S. Rubanov, S. E. Watkins, P. Mulvaney and J. J. Jasieniak, Layer-by-layer assembly of sintered $CdSe_xTe_{1-x}$ nanocrystal solar cells, *ACS Nano*, 2012, **6**(7), 5995.
18 S. Jeong, B.-S. Lee, S. Ahn, K. Yoon, Y.-H. Seo, Y. Choi and B.-H. Ryu, An 8.2% efficient solution-processed $CuInSe_2$ solar cell based on multiphase $CuInSe_2$ nanoparticles, *Energy Environ. Sci.*, 2012, **5**(6), 7539.
19 J. Jasieniak, B. I. MacDonald, S. E. Watkins and P. Mulvaney, Solution-processed sintered nanocrystal solar cells via layer-by-layer assembly, *Nano Lett.*, 2011, **11**(7), 2856.
20 J. B. Hoffman, G. Zaiats, I. Wappes and P. V. Kamat, $CsPbBr_3$ Solar Cells: Controlled film growth through layer-by-layer quantum dot deposition, *Chem. Mater.*, 2017, **29**(22), 9767.

21 R. A. Scheidt, C. Atwell and P. V. Kamat, Tracking transformative transitions: from $CsPbBr_3$ nanocrystals to bulk perovskite films, *ACS Mater. Lett.*, 2019, **1**(1), 8.

22 J. Hou, P. Chen, A. Shukla, A. Krajnc, T. Wang, X. Li, R. Doasa, L. H. G. Tizei, B. Chan, D. Johnstone, *et al.*, Liquid-phase sintering of lead halide perovskites and metal-organic framework glasses, *Science*, 2021, **374**(6567), 621.

23 S. Shrestha, R. Fischer, G. J. Matt, P. Feldner, T. Michel, A. Osvet, I. Levchuk, B. Merle, S. Golkar, H. Chen, *et al.*, High-performance direct conversion X-ray detectors based on sintered hybrid lead triiodide perovskite wafers, *Nat. Photonics*, 2017, **11**(7), 436.

24 N. J. Lóh, L. Simão, C. A. Faller, A. De Noni and O. R. K. Montedo, A review of two-step sintering for ceramics, *Ceram. Int.*, 2016, **42**(11), 12556.

25 I. W. Chen and X. H. Wang, Sintering dense nanocrystalline ceramics without final-stage grain growth, *Nature*, 2000, **404**(6774), 168.

26 Q. A. Akkerman, M. Gandini, F. Di Stasio, P. Rastogi, F. Palazon, G. Bertoni, J. M. Ball, M. Prato, A. Petrozza and L. Manna, Strongly emissive perovskite nanocrystal inks for high-voltage solar cells, *Nat. Energy*, 2016, **2**, 16194.

27 S. Zhou, G. Zhou, Y. Li, X. Xu, Y.-J. Hsu, J. Xu, N. Zhao and X. Lu, Understanding charge transport in all-inorganic halide perovskite nanocrystal thin-film field effect transistors, *ACS Energy Lett.*, 2020, **5**(8), 2614.

28 S.-E. Chiang, J.-R. Wu, H.-M. Cheng, C.-L. Hsu, J.-L. Shen, C.-T. Yuan and S. H. Chang, Origins of the S-shape characteristic in J–V curve of inverted-type perovskite solar cells, *Nanotechnology*, 2019, **31**(11), 115403.

29 E. Péan, S. Dimitrov, C. De Castroc and M. Davies, Interpreting time-resolved photoluminescence of perovskite materials, *Phys. Chem. Chem. Phys.*, 2020, **22**, 28345–28358.

30 M. Hoang, A. Pannu, Y. Yang, S. Madani, P. Shaw, P. Sonar, T. Tesfamichael and H. Wang, Surface Treatment of Inorganic $CsPbI_3$ Nanocrystals with Guanidinium Iodide for Efficient Perovskite Light-Emitting Diodes with High Brightness, *Nano-Micro Lett.*, 2022, **14**, 69.

31 C. Luo, Y. Zhao, X. Wang, F. Gao and Q. Zhao, Self-induced type-i band alignment at surface grain boundaries for highly efficient and stable perovskite solar cells, *Adv. Mater.*, 2021, **33**(40), 2103231.

32 C. Zhang, S. Mahadevan, J. Yuan, J. K. W. Ho, Y. Gao, W. Liu, H. Zhong, H. Yan, Y. Zou, S.-W. Tsang, *et al.*, Unraveling Urbach tail effects in high-performance organic photovoltaics: dynamic vs static disorder, *ACS Energy Lett.*, 2022, **7**(6), 1971.

33 B. Subedi, C. Li, C. Chen, D. Liu, M. M. Junda, Z. Song, Y. Yan and N. J. Podraza, Urbach energy and open-circuit voltage deficit for mixed anion–cation perovskite solar cells, *ACS Appl. Mater. Interfaces*, 2022, **14**(6), 7796.

34 J. Chantana, Y. Kawano, T. Nishimura, A. Mavlonov and T. Minemoto, Impact of Urbach energy on open-circuit voltage deficit of thin-film solar cells, *Sol. Energy Mater. Sol. Cells*, 2020, **210**, 110502.

35 S. De Wolf, J. Holovsky, S.-J. Moon, P. Löper, B. Niesen, M. Ledinsky, F.-J. Haug, J.-H. Yum and C. Ballif, Organometallic halide perovskites: sharp optical absorption edge and its relation to photovoltaic performance, *J. Phys. Chem. Lett.*, 2014, **5**(6), 1035.

36 M. Ledinský, A. Vlk, T. Schönfeldová, J. Holovský, E. Aydin, H. X. Dang, Z. Hájková, L. Landová, J. Valenta, A. Fejfar, *et al.*, Impact of cation multiplicity on halide perovskite defect densities and solar cell voltages, *J. Phys. Chem. C*, 2020, **124**(50), 27333.

37 A. Aytimur, S. Koçyiğit and İ. Uslu, Calcia stabilized ceria doped zirconia nanocrystalline ceramic, *J. Inorg. Organomet. Polym. Mater.*, 2014, **24**(6), 927.

38 M. Mazaheri, A. Simchi and F. Golestani-Fard, Densification and grain growth of nanocrystalline 3Y-TZP during two-step sintering, *J. Eur. Ceram. Soc.*, 2008, **28**(15), 2933.

39 R. M. Cannon and W. C. Carter, Interplay of sintering microstructures, driving forces, and mass transport mechanisms, *J. Am. Ceram. Soc.*, 1989, **72**(8), 1550.

40 F. Palazon, C. Urso, L. De Trizio, Q. Akkerman, S. Marras, F. Locardi, I. Nelli, M. Ferretti, M. Prato and L. Manna, Postsynthesis transformation of insulating Cs_4PbBr_6 nanocrystals into bright perovskite $CsPbBr_3$ through physical and chemical extraction of CsBr, *ACS Energy Lett.*, 2017, **2**(10), 2445.

41 Y. Mu, Z. He, K. Wang, X. Pi and S. Zhou, Recent Progress and Future Prospects on Halide Perovskite Nanocrystals for Optoelectronics and Beyond, *iScience*, 2022, **25**, 105371.

42 X. Ding, Y. Ren, Y. Wu, Y. Xu, J. Zhu, T. Hayat, A. Alsaedi, Z. Li, Y. Huang and S. Dai, Sequential deposition method fabricating carbon-based fully-inorganic perovskite solar cells, *Sci. China Mater.*, 2018, **61**, 73–79.

43 J. Duan, Y. Wang, X. Yang and Q. Tang, Alkyl-chain-regulated charge transfer in fluorescent inorganic $CsPbBr_3$ perovskite solar cells, *Angew. Chem., Int. Ed.*, 2020, **59**(11), 4391.

44 J. L. Duan, Y. Y. Zhao, X. Y. Yang, Y. D. Wang, B. L. He and Q. W. Tang, Lanthanide ions doped $CsPbBr_3$ halides for HTM-free 10.14%-efficiency inorganic perovskite solar cell with an ultrahigh open-circuit voltage of 1.594 V, *Adv. Energy Mater.*, 2018, **8**, 1802346.

45 J. Du, J. Duan, Y. Duan and Q. Tang, Tailoring organic bulk-heterojunction for charge extraction and spectral absorption in $CsPbBr_3$ perovskite solar cells, *Sci. China Mater.*, 2021, **64**, 798–807.